



HAL
open science

From Non-Model-Based to Adaptive Model-Based Tracking Control of Low-Inertia Underwater Vehicles

Auwal Tijjani Shehu, Ahmed Chemori

► **To cite this version:**

Auwal Tijjani Shehu, Ahmed Chemori. From Non-Model-Based to Adaptive Model-Based Tracking Control of Low-Inertia Underwater Vehicles. George M. Roman. Underwater Vehicles: Design and Applications, Chapter 2, , 2020, 978-1-53618-876-9. lirmm-03009836

HAL Id: lirmm-03009836

<https://hal-lirmm.ccsd.cnrs.fr/lirmm-03009836v1>

Submitted on 17 Nov 2020

HAL is a multi-disciplinary open access archive for the deposit and dissemination of scientific research documents, whether they are published or not. The documents may come from teaching and research institutions in France or abroad, or from public or private research centers.

L'archive ouverte pluridisciplinaire **HAL**, est destinée au dépôt et à la diffusion de documents scientifiques de niveau recherche, publiés ou non, émanant des établissements d'enseignement et de recherche français ou étrangers, des laboratoires publics ou privés.

*Chapter 1***FROM NON-MODEL-BASED TO ADAPTIVE
MODEL-BASED TRACKING CONTROL OF
LOW-INERTIA UNDERWATER VEHICLES***Auwal Shehu Tijjani and Ahmed Chemori**

LIRMM, University of Montpellier, CNRS, Montpellier, France.

Abstract

This chapter investigates the performances of different control schemes, from non-model-based (proportional-integral-derivative control, PID) to model-based (computed torque control, CT) as well as adaptive model-based (adaptive proportional-derivative plus control, APD+), implemented on a low-inertia underwater vehicle for three-dimensional (3D) helical trajectory tracking. Then, the asymptotic stability of the resulting closed-loop dynamics for each control scheme is proven based on the Lyapunov direct method. The performances of the control schemes, implemented on the Leonard underwater vehicle for 3D helical trajectory tracking, are then demonstrated through scenarios-based numerical simulations. The proposed simulations are conducted under the influences of the vehicle's buoyancy and damping changes, parametric variations; sensor noise, internal vehicle's perturbations; and water current, external disturbances rejection. Moreover, we demonstrate the task of transporting an object by the vehicle during underwater missions. The obtained simulation results show the effectiveness and robustness of the APD+ control scheme for tracking control of the low-inertia underwater vehicle in marine applications, outperforming the other controllers.

Keywords: Non-model-based control, model-based control, adaptive model-based control, computed torque control, PID, APD+, stability analysis, low-inertia underwater vehicle.

*LIRMM, University of Montpellier, CNRS, Montpellier, France. E-mail: Ahmed.Chemori@lirmm.fr

1 Introduction

1.1 Context

The high demand for raw materials on the land surface due to the rapid technological advances in industry and research activities broaden the exploration and exploitation of subsea environments. These raw materials includes: crude oil and natural gas, solid minerals (nickel, silver, copper, gold, cobalt etc), aquatic plants and animals [1]. Being an alternative natural source of raw materials currently and in the near future, approximately less than 10% of the subsea is explored and exploited by human either for civil or military purposes [2], [3], [4]. Some of the characteristics that make the subsea challenging to explore and exploit by the human despite its abundance deposit of raw materials include: poor visibility especially at higher depths, poor or impossible electromagnetic transmission which hinders online communications, highly dynamical and unstructured nature of the environment, as well as the impact of waves and water currents [5].

Being motivated by the challenges of the subsea as well as the high demand for raw materials, research communities proposed using divers for exploring and exploiting this environment. The proposed solution was associated to inherent challenges such as putting the lives of the divers at risk, the expensive cost, the time-consuming, the low efficiency, etc. Based on these limitations, other groups of research communities proposed using manned underwater vehicles (MUVs) for exploring and exploiting the subsea environment. Although the proposed idea was a big step forward, it was also associated with other challenges. For instance, when MUVs got stuck in a confined environment, the lives of the personnel inside will be at risk such as the real-life scenario happen with an MUV carrying seven personnel identified as *AS-28*. The vehicle was trapped 15 years ago by underwater radar cables in the pacific ocean at a depth of approximately 250m from the surface [5]. In view of the challenges faced by MUVs, with the recent technological advances in computational power of microprocessors, sensors, battery systems and vision system, unmanned underwater vehicles (UUVs) are becoming the ultimate tool for exploring and exploiting subsea environments [6].

In general, UUVs can be classified into remotely operated underwater (ROVs) and autonomous underwater vehicles (AUVs) [6]. During the exploration and exploitation of the subsea, either for the civil or military purposes, the mission may involve operations such as seafloor mapping, drilling, monitoring, inspection, debris cleaning, search and rescue, etc. These missions may require the ability of the vehicle to make autonomously an intelligent decision. The autonomous behaviours for instance could be station keeping, spatial trajectory tracking, collision avoidance, desired velocity profile regulation, and so on [7], [8]. The presence of intelligent behaviour in AUV broadens its operational context in subsea missions [7]. In this chapter, we will focus on the case spatial trajectory tracking. Even though designing an onboard control scheme combining several autonomous behaviours for AUVs remains a challenging task and an open research problem.

1.2 Related Work

Despite, the challenge of designing an onboard control scheme for AUVs, various contributions have been proposed by several research communities to resolve the problems of station keeping, spatial trajectory tracking, collision avoidance, desired velocity profile regulation and classical path-following. Focusing on trajectory tracking and station keeping problems, some of the proposed classical non-model-based controllers include: classical PD and PID control schemes for position and velocity regulation, respectively, of a fully actuated AUVs, that have been proposed in [9]. Even though the authors focused the work on control design and the stability analysis, the analytical stability analysis of the control schemes designed are not conducted. Similarly, in [10], the authors demonstrated the application of a PID control scheme for depth motion control of micro-AUVs swarms through simulation and real-time experiment. However, the obtained results show that the PID control scheme is oscillatory at steady-state. For this reason, the authors proposed a bounded PD control scheme to deal with this effect, and the proposed control scheme was validated through simulations and real-time experiments. A real-time station keeping problem was also addressed in [11] using classical PID control. Moreover, the depth and heading control using a classical PID control scheme for Amogh AUV has been proposed in [12].

Although PID control scheme demonstrated some level of AUV's tracking control performance in the literature, keeping in mind the dynamical nature of the subsea and the vehicle's dynamics nonlinearity, this non-model-based control scheme will certainly not be able to solve all the trajectory tracking and station keeping problems for AUVs especially in high precision applications. For this reason, improved non-model-based control schemes such as fuzzy logic-based PID [13, 14], GA-based PID [15], saturation-based nonlinear PD/PID [16], classical RISE control, etc. have been proposed. To improve the performance of the classical PID controller for tracking control of mini-ROVs in subsea applications, the idea of auto-adjustment of the feedback gains using neural networks has been proposed in [17]. Although the authors demonstrated the performance of the control scheme through simulations and real-time experiments, the neural networks are always associated with long training time and high computational cost. Also, in [18], PID control approach has been proposed for depth and yaw tracking of UUVs. To improve the performance of the PID, the authors proposed using fuzzy gain scheduling to design the controller at various operating points with optimal gains.

So far, the improved non-model-based controllers show superior performance over classical non-model-based controllers, such as classical PD and PID in trajectory tracking and station keeping for UUVs; however, having some knowledge about the AUVs dynamics will certainly help to improve the performance of the designed control scheme for these vehicles. Consequently, model-based classical control (saturation-based nonlinear fractional order PD, nonlinear PD based on variable saturation function, etc.) as well as model-based robust control (nonlinear RISE, sliding mode, high-order sliding mode, etc.) have been investigated in [19], [20] and [21], [22] respectively. Also, in [23] exact linearisation and nonlinear model-based controllers have been proposed for set-point regulation and trajectory tracking tasks. The performances of the proposed control schemes are evaluated through real-time experiments using Johns Hopkins University remotely operated vehicle (JHU-ROV). However, the computational time of the proposed controllers can be reduced using

desired compensation in the control schemes, which could be computed offline. Similarly, a nonlinear model-based controller for six degrees of freedom position and velocity tracking has been proposed in [24]. The control scheme has been implemented on the fully actuated JHU-ROV through both numerical simulations and real-time experiments. The obtained results show the better performance of the nonlinear model-based controller when compared with a non-model-based controller. A robust fuzzy controller for ROVs has been proposed by [25]. In the control scheme, the membership functions are adjusted using genetic algorithms, which modified the gains of the controller based on the task complexity assigned to the ROV. Similarly, an optimised fuzzy controller for path tracking of an underwater vehicle has been proposed in [26], and validated experimentally on Sea-Dog underwater vehicle. Also, three-dimensional spatial tracking control of a hybrid AUVs under the influence of underwater currents has been addressed in [27].

In spite of the notable performances of model-based robust control schemes, in some subsea missions, their performances may be degraded drastically due to inherent uncertainties in subsea environments, as well as in the vehicles themselves. To deal with these effects, several research communities proposed using control schemes able to dynamically adjust themselves in real-time. Indeed, the proposed idea opens another interesting field of research known as adaptive control; based on the notion that the auto-adjustment will not only maintain but also improve the desired control system performance.

In the context of underwater vehicles, adaptive control schemes have been proposed by several research studies. For instance, an adaptive thruster fault tolerant region tracking control with prescribed transient performance has been investigated in [28]. Even though factors such as thruster fault, measurement noise, parameter uncertainties and underwater currents were considered; additional cases could be added to ascertain the effectiveness of the proposed scheme. Similarly, adaptive tracking control and its improvement using a disturbance observer for underwater vehicles have been proposed in [29] and [8] respectively. Besides, a variable forgetting factor model-free adaptive control for surface unmanned vehicles has been studied in [30]; this scheme could be extended to the case of UUVs. Output constraints fuzzy-based adaptive tracking control for autonomous underwater vehicles was investigated in [31]; where numerical simulations were carried out to show the effectiveness of the proposed scheme. Adaptive formation control based on output-feedback for an under-actuated surface vehicle has been proposed in [32]. However, this scheme does not consider measurement noise. In [33], an indirect adaptive control scheme for intervention operations of AUV has been proposed. The robustness of the control scheme is enhanced with an extended Kalman filter (EKF), which is used to take care of external disturbances, parametric uncertainties, payload variations, sensor noise and actuator nonlinearity. Despite the proposed complex adaptive control schemes in the literature, still classical adaptive schemes dominating the majority of real-time marine applications.

1.3 Chapter Contribution and Organisation

In this chapter, we propose to investigate design, stability analysis and effectiveness of tracking control schemes, from non-model-based to model-based as well as adaptive model-based and their application to control a low-inertia underwater vehicle for marine missions. These vehicles are characterised with high power to weight ratio, which makes them vul-



Figure 1: View of Leonard underwater vehicle thrusters' allocation, which produces forces responsible for the navigation of the vehicle.

nerable toward any slight variation in the system parameter.

The remaining parts of this chapter are organised as follow. In section 2, the low-inertia underwater vehicle description as well as its six-degree-of-freedom modelling are introduced. Then, section 3 is devoted to the proposed tracking control schemes and their stability analysis. Numerical simulation results are presented and discussed in section 4, while section 5 finalises the chapter with some concluding remarks and future works.

2 Vehicle Description and Modelling

2.1 Vehicle Description

To validate our proposed investigations in this chapter, we perform numerical simulation using a LIRMM's underwater vehicle known as Leonard. Even though some specific features of this vehicle are well described in [34] and [8]; we recall some of these essential features again to facilitate kinematics and dynamics formulations of the vehicle in this chapter. The vehicle can be categorised as a low-inertia hybrid underwater vehicle, that is, having both remote and autonomous operation capabilities. Additionally, being a holonomic system can be suitable for various marine missions. The vehicle's translational and rotational motions are determined by its thrusters' allocation illustrated in Figure 1.

Besides, the vehicle is equipped with six thrusters, energy consumption is minimised by keeping neutrally both the vehicle's pitch and roll close to zero with respect to the horizontal. Table 1 summarises some of the vehicle's hardware components, as well as its parameters.

Table 1: The main technical specifications of Leonard low-inertia underwater vehicle

Hardware Components and Parameters	Descriptions
Attitude Sensor	Sparkfun MPU 9250, MEMS 9-axes gyrometer, accelerometer and magnetometer microprocessor.
Depth Sensor	MS5803-14BA (Pressure Sensor).
Dimensions	0.75m (l) \times 0.55m (w) \times 0.45m (h).
Floatability	9N.
Mass	28kg.
Maximal Depth	100m.
Power	48V - 600W.
Sampling Period	0.05s.
Tether Length	150m.
Thrusters	6-Seabotix BTD150.

2.2 Vehicle Modelling in Six Degrees of Freedom

The kinematics and dynamics of a low-inertial underwater vehicle such as Leonard can be derived with respect to 3D reference frames. These frames are the earth-fixed and the body-fixed frames. Figure 2 illustrates the frames assignment, for guidance and navigation of Leonard underwater vehicle, using SNAME (Society of Naval Architects and Marine Engineers) standard [34].

2.2.1 Vehicle kinematics in six degrees of freedom

For a rigorous kinematic formulation based on Figure 2, we can express the time derivatives of the vehicle's position and orientation in the earth-fixed frame with respect to its linear and angular velocities in vehicle's body-fixed frame as follows:

$$\dot{\eta} = J(\eta)v \quad (1)$$

where $v = [v_1 \ v_2]^T$ is the vector of linear and angular velocities in the body-fixed frame, $v_1 = [u \ v \ w] \in \mathbb{R}^{3 \times 1}$ and $v_2 = [p \ q \ r] \in \mathbb{R}^{3 \times 1}$, $\eta = [\eta_1 \ \eta_2]^T$ denotes the vector of position and orientation in the earth-fixed frame, $\eta_1 = [x \ y \ z] \in \mathbb{R}^{3 \times 1}$ and $\eta_2 = [\phi \ \theta \ \psi] \in \mathbb{R}^{3 \times 1}$, while $J(\eta) \in \mathbb{R}^{6 \times 6}$ is a matrix of the 3D spatial transformation between the earth-fixed frame and body-fixed frame.

This transformation matrix $J(\eta)$ is given by [35]:

$$J(\eta) = \begin{bmatrix} J_1(\eta_2) & 0_{3 \times 3} \\ 0_{3 \times 3} & J_2(\eta_2) \end{bmatrix} \quad (2)$$

where $J(\eta_1)$ and $J(\eta_2)$ are given by (3) and (4) respectively, as follows (see [35] for further details):

$$J_1(\eta_2) = \begin{bmatrix} c\psi c\theta & c\psi s\theta s\phi - s\psi c\phi & c\psi s\theta c\phi + s\psi s\phi \\ s\psi c\theta & s\psi s\theta s\phi + c\psi c\phi & s\psi s\theta c\phi - c\psi s\phi \\ -s\theta & c\theta s\phi & c\theta c\phi \end{bmatrix} \quad (3)$$

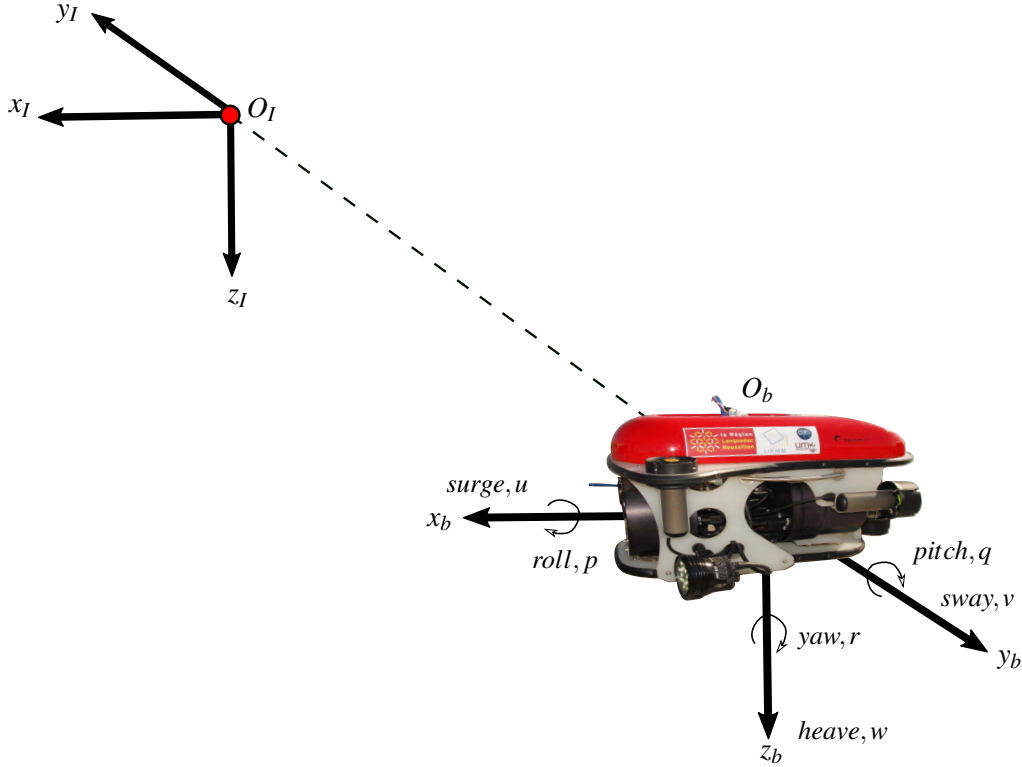


Figure 2: Illustration of the earth-fixed frame (O_I, x_I, y_I, z_I) and the body-fixed frame (O_b, x_b, y_b, z_b) frames assignment for kinematic and dynamic modelling.

$$J_2(\eta_2) = \begin{bmatrix} 1 & s\psi t\theta & c\psi t\theta \\ 0 & c\psi & -s\psi \\ 0 & s\phi/c\theta & c\phi/c\theta \end{bmatrix} \quad (4)$$

with c angle, s angle and t angle representing \cos angle, \sin angle and \tan angle functions respectively, where angle = $\phi = \theta = \psi$.

2.2.2 Vehicle dynamics in six degrees of freedom

Many research studies have well described the dynamics of an underwater vehicle [34], [5]. Inspired by these research studies and representation proposed by [35], the dynamics describing the motion of our underwater vehicle, based on SNAME notations in the vehicle's body-fixed frame, can be written as follows:

$$M\dot{\mathbf{v}} + C(\mathbf{v})\mathbf{v} + D(\mathbf{v})\mathbf{v} + \mathbf{g}(\boldsymbol{\eta}) = \boldsymbol{\tau} + \mathbf{w}_{ext}(t) \quad (5)$$

where $M \in \mathbb{R}^{6 \times 6}$ defines the inertia matrix including the added mass effects, $C(\mathbf{v}) \in \mathbb{R}^{6 \times 6}$ represents the Coriolis and centripetal matrix, $D(\mathbf{v}) \in \mathbb{R}^{6 \times 6}$ is the hydrodynamic damping matrix including both linear and quadratic effects, $\mathbf{g}(\boldsymbol{\eta}) \in \mathbb{R}^{6 \times 1}$ defines the vector of restoring forces and moments, $\boldsymbol{\tau} \in \mathbb{R}^{6 \times 1}$ represents the vector of control inputs and $\mathbf{w}_{ext}(t) \in \mathbb{R}^{6 \times 1}$ is the vector of time-varying external disturbances.

Additionally, the matrices and vectors defined in the vehicle's dynamics (5) are described as follows:

The total contributions of the vehicle's rigid-body inertia, M_{RB} and the inertia of the added mass, M_A constitute the so called inertia matrix M . This matrix can be written as:

$$M = M_{RB} + M_A \quad (6)$$

Based on the assumption that we consider the motion of the vehicle at low-speed, the matrix M can be simplified as follows:

$$M = \text{diag}\{m + X_{\dot{u}}, m + Y_{\dot{v}}, m + Z_{\dot{w}}, I_{xx} + K_{\dot{p}}, I_{yy} + M_{\dot{q}}, I_{zz} + N_{\dot{r}}\} \quad (7)$$

where m is the mass of the vehicle, $\{I_{xx}, I_{yy}, I_{zz}\}$ are the vehicle's rigid-body moments of inertia and $\{X_{\dot{u}}, Y_{\dot{v}}, Z_{\dot{w}}, K_{\dot{p}}, M_{\dot{q}}, N_{\dot{r}}\}$ are the hydrodynamics added masses.

Similarly, the Coriolis and centripetal matrix is usually expressed as (see [35] for more details):

$$C(\mathbf{v}) = C_{RB}(\mathbf{v}) + C_A(\mathbf{v}) \quad (8)$$

where $C_{RB}(\mathbf{v})$ and $C_A(\mathbf{v})$ denote the Coriolis and centripetal (rigid-body and hydrodynamics) matrices, which are given by (9) and (10) as follows:

$$C_{RB}(\mathbf{v}) = \begin{bmatrix} 0 & -mr & mq & 0 & 0 & 0 \\ mr & 0 & -mp & 0 & 0 & 0 \\ -mq & mp & 0 & 0 & 0 & 0 \\ 0 & 0 & 0 & 0 & I_{zz}r & -I_{yy}q \\ 0 & 0 & 0 & -I_{zz}r & 0 & I_{xx}p \\ 0 & 0 & 0 & I_{yy}q & -I_{xx}p & 0 \end{bmatrix} \quad (9)$$

$$C_A(\mathbf{v}) = \begin{bmatrix} 0 & 0 & 0 & 0 & -Z_{\dot{w}}w & Y_{\dot{v}}v \\ 0 & 0 & 0 & Z_{\dot{w}}w & 0 & -X_{\dot{u}}u \\ 0 & 0 & 0 & -Y_{\dot{v}}v & X_{\dot{u}}u & 0 \\ 0 & -Z_{\dot{w}}w & Y_{\dot{v}}v & 0 & -N_{\dot{r}}r & M_{\dot{q}}q \\ Z_{\dot{w}}w & 0 & -X_{\dot{u}}u & N_{\dot{r}}r & 0 & -K_{\dot{p}}p \\ -Y_{\dot{v}}v & X_{\dot{u}}u & 0 & -M_{\dot{q}}q & K_{\dot{p}}p & 0 \end{bmatrix} \quad (10)$$

The detail step-by-step process of obtaining approximate values of the hydrodynamics elements ($X_u, Y_v, Z_w, K_p, M_q, N_r$) of the vehicle's $D(\mathbf{v})$ matrix is addressed in [34]. Considering the low-speed motion of the vehicle, we can approximate the damping matrix $D(\mathbf{v})$ as follows:

$$D(\mathbf{v}) = \text{diag}\{X_u, Y_v, Z_w, K_p, M_q, N_r\} \quad (11)$$

Concerning the restoring forces and moments $g(\boldsymbol{\eta})$, we assume that the centre of gravity coincides with the centre of the vehicle; as a result, the vector $g(\boldsymbol{\eta})$ can be written as:

$$g(\boldsymbol{\eta}) = \begin{bmatrix} f_b s \theta \\ -f_b c \theta s \psi \\ -f_b c \theta c \psi \\ -z_{cb} B c \theta s \psi \\ -z_{cb} B s \theta \\ 0 \end{bmatrix} \quad (12)$$

where $B = \text{Buoyancy}$, while f_b and z_{cb} are the buoyancy force and the position of the centre of buoyancy of the vehicle, respectively.

We finalise the description of the vehicle's dynamics terms with τ , which is a control inputs vector responsible for the translational and rotational motions of the vehicle. A particular motion pattern is possible through actuating a precise vehicle's thrusters configuration. The control input vector τ can be written as follows:

$$\tau = B^* \cdot F^* \quad (13)$$

where $B^* \in \mathbb{R}^{6 \times 6}$ is the thrusters' allocation matrix, which maps all the control inputs to their corresponding forces and moments for translational and rotational motions of the vehicle, and $F^* = [F_1 \ F_2 \ F_3 \ F_4 \ F_5 \ F_6]^T$ is a vector of the forces generated by the six thrusters of the vehicle.

3 Proposed Control Solutions and their Stability Analysis

3.1 Control Solution 1: A Non-model-based Tracking Control Scheme

A control scheme that can be designed based only on the system states is referred to as a non-model-based control scheme [36]. It does not require any prior information on the system dynamics. There are many control schemes proposed in the literature based on non-model-based structures. However, the most famous scheme, widely used in industry, is the conventional proportional-integral-derivative (PID) control scheme. Besides its implementation simplicity, this approach scheme works satisfactorily in many industrial applications [37]. Regarding low-inertia underwater water vehicles, PID and PD control schemes have widely been used in most of the real-time marine applications [38], [16]; therefore in this section, we focus on the control structure based on the PID algorithm as our non-model-based control scheme case study.

3.1.1 Background on PID control scheme

The classical PID control scheme has the following structure:

$$U(t) = K_p e(t) + K_i \int_0^t e(\sigma) d\sigma + K_d \left[\frac{de(t)}{dt} \right] \quad (14)$$

where $U(t)$ is the control signal, $e(t)$ defines the error signal, which is obtained as the difference between the reference signal $r(t)$ and output to be controlled $y(t)$, while K_p , K_i and K_d are respectively the proportional, integral and derivative feedback gains of the controller. Even though the feedback gains can be selected easily during the implementation of the control scheme, the selection of optimal feedback gains is a nontrivial task. Where each gain has a particular effect on the system's behaviour; for instance, an optimal value of K_p decreases the response time and steady-state error of the closed-loop system, optimal K_i value removes steady-state error and K_d improves the stability through increasing the damping of the resulting closed-loop dynamics.

On the other hand, non-optimal gains selection may lead to the instability of the resulting closed-loop dynamics. Several techniques have been proposed in the literature for a relevant tuning of these feedback gains (see for instance, [39]).

3.1.2 Application of the PID on Leonard underwater vehicle

We proposed to apply the classical PID structure given by (14) to our nonlinear coupled six degrees of freedom underwater vehicle described in (5). The controller is aimed to guide the vehicle to track the desired trajectories defined as follows:

$$\eta_d(t) = [x_d(t), y_d(t), z_d(t), \phi_d(t), \theta_d(t), \psi_d(t)]^T \quad (15)$$

If we write the vehicle's trajectories as:

$$\eta(t) = [x(t), y(t), z(t), \phi(t), \theta(t), \psi(t)]^T \quad (16)$$

Then, the tracking error $e(t)$ can be expressed as follows:

$$e(t) = \eta(t) - \eta_d(t) \quad (17)$$

where $e(t)$ is a vector of the tracking errors of all the six degrees of freedom, and is expressed as, $e(t) = [e_1(t), e_2(t), \dots, e_6(t)]^T$, while $\eta_d(t)$ and $\eta(t)$ are the desired and actual trajectories given by (15) and (16), respectively.

The control input vector τ to be applied to our underwater vehicle is designed as follows:

$$\tau = -J^T(\eta)[\tau_{PID}] \quad (18)$$

where, the PID control law τ_{PID} can be expressed as follows:

$$\tau_{PID} = K_p e(t) + K_i \int_0^t e(\sigma) d\sigma + K_d \left[\frac{de(t)}{dt} \right] \quad (19)$$

where $\tau = [\tau_x, \tau_y, \tau_z, \tau_\phi, \tau_\theta, \tau_\psi]^T$ is the vector of the control inputs for all the six degrees of freedom, $e(t)$ is the vector of the tracking errors, while $K_p = \text{diag}\{k_{1p}, k_{2p}, \dots, k_{6p}\} > 0$, $K_i = \text{diag}\{k_{1i}, k_{2i}, \dots, k_{6i}\} > 0$ and $K_d = \text{diag}\{k_{1d}, k_{2d}, \dots, k_{6d}\} > 0$ are the PID feedback gains matrices.

The above designed PID-based control scheme can be illustrated by the block diagram of Figure 3.

3.1.3 Stability analysis

To facilitate the stability analysis, let us consider the transformation of (5) into the earth-fixed frame (O_I, x_I, y_I, z_I) using (1) as follows:

$$M^*(\eta)\ddot{\eta} + C^*(v, \eta)\dot{\eta} + D^*(v, \eta)\dot{\eta} + g^*(\eta) = \tau^*(\eta) + w_{ext}(t) \quad (20)$$

where

$$M^*(\eta) = J^{-T}(\eta)MJ^{-1}(\eta),$$

$$C^*(v, \eta) = J^{-T}(\eta)[C(v) - MJ^{-1}(\eta)J(\eta)]J^{-1}(\eta),$$

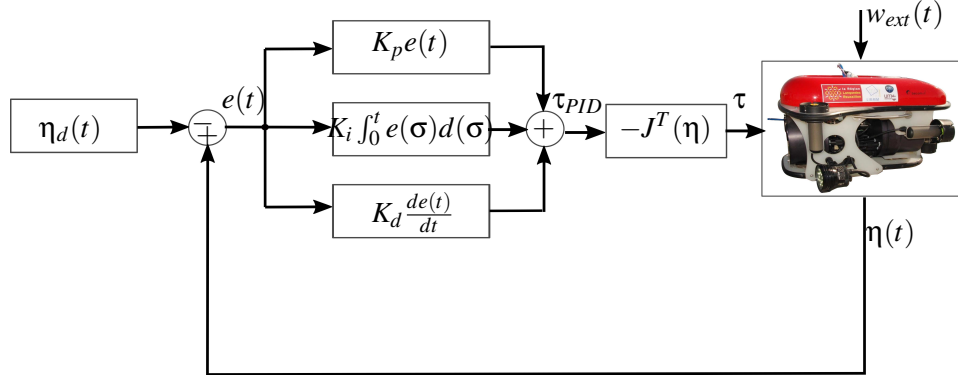


Figure 3: Block diagram of the non-model-based PID control scheme implemented on Leonard underwater vehicle.

$$D^*(\mathbf{v}, \boldsymbol{\eta}) = J^{-T}(\boldsymbol{\eta})D(\mathbf{v})J^{-1}(\boldsymbol{\eta}),$$

$$g^*(\boldsymbol{\eta}) = J^{-T}(\boldsymbol{\eta})g(\boldsymbol{\eta}),$$

$$\boldsymbol{\tau}^*(\boldsymbol{\eta}) = J^{-T}(\boldsymbol{\eta})\boldsymbol{\tau}$$

Assumption 1: The external disturbance $w_{ext}(t)$, including water waves and currents, is assumed to be Lipschitz continuous. Also, its time derivative exists and is bounded: $|\dot{w}_{i_{ext}}(t)| \leq L_i, i = \overline{1,6}$.

Substituting (18) into (20), yields:

$$M^*(\boldsymbol{\eta})\ddot{\boldsymbol{\eta}} = -C^*(\mathbf{v}, \boldsymbol{\eta})\dot{\boldsymbol{\eta}} - D^*(\mathbf{v}, \boldsymbol{\eta})\dot{\boldsymbol{\eta}} - g^*(\boldsymbol{\eta}) + w_{ext}(t) - \boldsymbol{\tau}_{PID} \quad (21)$$

Before substituting (19) into (21), the integral term of $\boldsymbol{\tau}_{PID}$ introduces an auxiliary state variable, which leads to the modification of (19) as follows:

$$\boldsymbol{\tau}_{PID} = K_p e + K_i \boldsymbol{\zeta} + K_d \dot{e} \quad (22)$$

where, $\boldsymbol{\zeta} = \int_0^t e(\boldsymbol{\sigma})d\boldsymbol{\sigma}$ is the auxiliary state variable and \dot{e} is the time derivative of (17). Then, we can adopt the following change of variable [40]:

$$z = a\boldsymbol{\zeta} + e \quad (23)$$

where $a > 0$ and $z = [z_1, z_2, \dots, z_6]^T$.

Using this change of variable, (22) can be rewritten as follows:

$$\boldsymbol{\tau}_{PID} = K_p^* e + K_i^* z + K_d \dot{e} \quad (24)$$

where $K_p^* = K_p - \frac{1}{a}K_i$ and $K_i^* = \frac{1}{a}K_i$.

By substituting (24) into (21), the resulting vehicle's closed-loop dynamics can be rewritten as follows:

$$\ddot{\boldsymbol{\eta}} = M^*(\boldsymbol{\eta})^{-1}[-C^*(\mathbf{v}, \boldsymbol{\eta})\dot{\boldsymbol{\eta}} - D^*(\mathbf{v}, \boldsymbol{\eta})\dot{\boldsymbol{\eta}} - g^*(\boldsymbol{\eta}) + w_{ext}(t) - K_p^* e - K_i^* z - K_d \dot{e}] \quad (25)$$

Then, (25) can be written in state-space form with a unique equilibrium point as follows:

$$\frac{d}{dt} \begin{bmatrix} e \\ \dot{e} \\ z \end{bmatrix} = \begin{bmatrix} \dot{e} \\ M^*(\boldsymbol{\eta})^{-1}[-C^*(\mathbf{v}, \boldsymbol{\eta})\dot{\boldsymbol{\eta}} - D^*(\mathbf{v}, \boldsymbol{\eta})\dot{\boldsymbol{\eta}} - g^*(\boldsymbol{\eta}) + w_{ext}(t) - K_p^* e - K_i^* z - K_d \dot{e}] - \ddot{\boldsymbol{\eta}}_d \\ ae + \dot{e} \end{bmatrix} \quad (26)$$

To guarantee the stability of the unique equilibrium point of this state-space model, we propose to use the Lyapunov direct method by considering the following Lyapunov candidate function:

$$V(e, \dot{e}, z) = \frac{1}{2} \dot{e}^T M^*(\eta) \dot{e} + [g^{*T}(\eta) + \dot{\eta}_d^T D^*(v, \eta)] e + \int_0^e z^T K_p^* dz + \int_0^e z^T K_i^* dz \quad (27)$$

To prove that $V(e, \dot{e}, z)$ is a positive definite function and radially unbounded, the term $\frac{1}{2} \dot{e}^T M^*(\eta) \dot{e}$ is positive definite, since $M^*(\eta)$ is a positive definite matrix; also, in the second term $D^*(v, \eta) > 0$ and it is possible to design η_d such that $\dot{\eta}_d > 0$. For the integral terms, we consider the following arguments [16]:

$$\int_0^e z^T K_p^* dz = \int_0^{e_1} z_1^T k_{1p}^* dz_1 + \int_0^{e_2} z_2^T k_{2p}^* dz_2 + \dots + \int_0^{e_6} z_6^T k_{6p}^* dz_6 \quad (28)$$

$$\int_0^e z^T K_p^* dz > 0, \quad \forall e \neq 0 \in \mathbb{R}^n \quad (29)$$

where $K_p^* = \text{diag}\{k_{1p}^*, k_{2p}^*, \dots, k_{6p}^*\}$.

From the arguments (28) and (29), we can deduce that:

$$\int_0^e z^T K_p^* dz \rightarrow \infty \quad \text{as } \|e\| \rightarrow \infty \quad (30)$$

Similarly, it is possible to apply the same above arguments to the second integral term of $V(e, \dot{e}, z)$ as follows:

$$\int_0^e z^T K_i^* dz > 0, \quad \forall e \neq 0 \in \mathbb{R}^n \quad (31)$$

leading to

$$\int_0^e z^T K_i^* dz \rightarrow \infty \quad \text{as } \|e\| \rightarrow \infty \quad (32)$$

From (27), the time derivative of $V(e, \dot{e}, z)$ can be expressed as follows:

$$\dot{V}(e, \dot{e}, z) = \dot{e}^T M^*(\eta) \ddot{e} + \frac{1}{2} \dot{e}^T \dot{M}^*(\eta) \dot{e} + e^T K_p^* \dot{e} + z^T K_i^* \dot{e} + g^{*T}(\eta) \dot{e} + \dot{\eta}_d^T D^*(v, \eta) \dot{e} \quad (33)$$

Injecting the closed-loop state-space dynamics (26) into (33), yields:

$$\begin{aligned} \dot{V}(e, \dot{e}, z) = & -\dot{e}^T C^*(v, \eta) \dot{\eta} - \dot{e}^T D^*(v, \eta) \dot{\eta} - \dot{e}^T g^*(\eta) + \dot{e}^T w_{ext}(t) - \dot{e}^T K_p^* e \\ & - \dot{e}^T K_i^* z - \dot{e}^T K_d \dot{e} - \dot{e}^T M^*(\eta) \ddot{\eta}_d + \frac{1}{2} \dot{e}^T \dot{M}^*(\eta) \dot{e} + e^T K_p^* \dot{e} + z^T K_i^* \dot{e} \\ & + g^{*T}(\eta) \dot{e} + \dot{\eta}_d^T D^*(v, \eta) \dot{e} \end{aligned} \quad (34)$$

Assumption 2: In this work, we consider that our vehicle moves at a low speed.

Based on Assumption 2, $\dot{M}^*(\eta) = 0$ and $C^*(v, \eta) \approx 0$, therefore (34) can be rewritten as follows:

$$\dot{V}(e, \dot{e}, z) = -\dot{e}^T D^*(v, \eta) \dot{e} - [\dot{e}^T K_d \dot{e} + \dot{e}^T M^*(\eta) \ddot{\eta}_d - \dot{e}^T w_{ext}(t)] \quad (35)$$

From (35), if we consider Assumption 1, it is always possible to design K_d of the controller to compensate for the effect of $w_{ext}(t)$ as follows:

$$K_{id} > \frac{\|w_{ext}(t)\| - \|M^*(\eta)\ddot{\eta}_d\|}{\|\dot{e}\|} \quad i = \overline{1,6} \quad (36)$$

where $K_d = \text{diag}\{k_{1d}, k_{2d}, \dots, k_{6d}\}$

Also, from (35) we can deduce that $\dot{e}^T D^*(v, \eta) \dot{e} > 0$, since $D^*(v, \eta) > 0$. Therefore, if (36) is satisfied, then $\dot{\eta}^T D^*(v, \eta) \dot{\eta}$ will dominate the right-hand side of (35). Consequently, we can conclude that $\dot{V}(e, \dot{e}, z)$ in (35) is negative semidefinite. In accordance with the LaSalle's invariance principle, the origin of the resulting closed-loop dynamics is asymptotically stable [34], [40].

Remark 1: Even though the PID controller proposed here is non-model-based, the process of tuning of its feedback gains is a nontrivial task. It can be noticed in (36) that having some knowledge of the system dynamics (for instance, inertia matrix $M^*(\eta)$ in our case) may help to select better PID feedback gains, which could improve the overall performance of the controller.

3.2 Control Solution 2: A Model-based Tracking Control Scheme

In various marine missions, the performance of non-model-based controllers is degraded due to external disturbances and parametric variations. Certainly, integrating the system dynamics (partially or entirely) into a non-model-based controller structure will help to improve its performance. Therefore, when a non-model-based control scheme contains the dynamics (partially or entirely) of the system it is known as a model-based control scheme [36]. However, obtaining accurate and simple dynamics of a system, having all the properties of the real system remains a challenging task. Concerning the control of our low-inertia underwater vehicle, we propose to focus our study on the computed torque (CT) control as an example of a model-based control scheme, which is based on the full knowledge of the vehicle's dynamics.

3.2.1 Background on the CT control and its application on Leonard underwater vehicle

The majority of the real systems are represented mathematically by nonlinear differential equations which mainly result in a nonlinear closed-loop dynamics, when controlled with model-based controllers. However, the CT control scheme has the advantage of transforming the closed-loop dynamics of the nonlinear system into a linear open-loop dynamics. As a result, we can use linear systems design tools to analyse the resulting linear closed-loop dynamics. Additionally, the CT controller can fulfil the tracking control objective without necessary an optimal tuning of the feedback gains [40]. For the tracking control of Leonard underwater vehicle, we propose to design the CT controller as follows:

$$\tau = J^T(\eta) \left[M^*(\eta) \ddot{\eta}_d + C^*(v, \eta) \dot{\eta} + D^*(v, \eta) \dot{\eta} + g^*(\eta) - M^*(\eta) \left[K_p e(t) + K_d \frac{de(t)}{dt} \right] \right] \quad (37)$$

where $\tau = [\tau_x, \tau_y, \tau_z, \tau_\theta, \tau_\psi]^T$ is the vector of the control inputs for all the six degrees of freedom of the vehicle, $J(\eta)$ is the transformation matrix, defined above, $e(t)$ is the vector of the tracking errors, $K_p = \text{diag}\{k_{1p}, k_{2p}, \dots, k_{6p}\} > 0$ and $K_d = \text{diag}\{k_{1d}, k_{2d}, \dots, k_{6d}\} > 0$ are the feedback gains, $M^*(\eta)$ defines the inertia matrix including the added mass effects, $C^*(v, \eta)$ represents the Coriolis and centripetal matrix, $D^*(v, \eta)$ is the hydrodynamic damping matrix including both linear and quadratic effects, and $g^*(\eta)$ defines the vector of restoring forces and moments.

Indeed, the terms $M^*(\eta)$, $C^*(v, \eta)$, $D^*(v, \eta)$ and $g^*(\eta)$ in the CT control law (37) are obtained from the vehicle's dynamics (20). The block diagram of the CT controller structure implemented on Leonard underwater vehicle is illustrated in Figure 4.

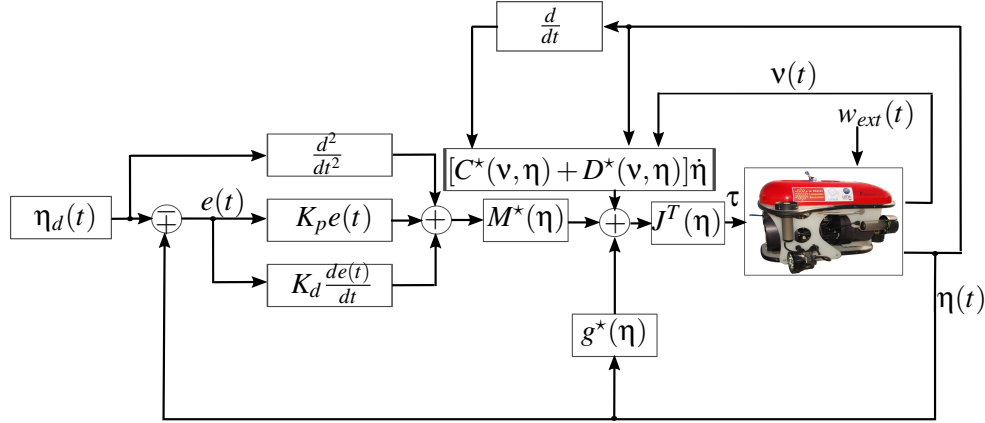


Figure 4: Block diagram of model-based CT control scheme implemented on Leonard underwater vehicle.

3.2.2 Stability analysis

To facilitate the stability analysis, let us begin by injecting the CT control law (37) into the vehicle's dynamics (20), resulting in:

$$M^*(\eta)\ddot{\eta} + C^*(v, \eta)\dot{\eta} + D^*(v, \eta)\dot{\eta} + g^*(\eta) = M^*(\eta)\ddot{\eta}_d + C^*(v, \eta)\dot{\eta} + D^*(v, \eta)\dot{\eta} + g^*(\eta) - M^*(\eta) \left[K_p e(t) + K_d \frac{de(t)}{dt} \right] + w_{ext}(t) \quad (38)$$

Then, we can rewrite the above closed-loop dynamics in the state-space form as follows:

$$\frac{d}{dt} \begin{bmatrix} e \\ \dot{e} \end{bmatrix} = \begin{bmatrix} \dot{e} \\ M^*(\eta)^{-1} w_{ext}(t) - K_p e - K_d \dot{e} \end{bmatrix} \quad (39)$$

Next, we can use the Lyapunov direct method to prove the stability of the resulting closed-loop dynamics by considering the following Lyapunov candidate function:

$$V(e, \dot{e}) = \frac{1}{2} \dot{e}^T \dot{e} + \int_0^e \alpha^T K_p d\alpha \quad (40)$$

The proposed Lyapunov candidate function is positive definite and radially unbounded since $\frac{1}{2}\dot{e}^T M^*(\eta)\dot{e}$ is positive definite, and the integral term satisfies the following arguments:

$$\int_0^e \alpha^T K_p d\alpha = \int_0^{e_1} \alpha_1^T k_{1p} d\alpha_1 + \int_0^{e_2} \alpha_2^T k_{2p} d\alpha_2 + \dots + \int_0^{e_6} \alpha_6^T k_{6p} d\alpha_6 \quad (41)$$

$$\int_0^e \alpha^T K_p d\alpha > 0, \quad \forall e \neq 0 \in \mathbb{R}^n \quad (42)$$

where $K_p = \text{diag}[k_{1p}, k_{2p}, \dots, k_{6p}]$.

From the above arguments (41) and (42), we can deduce that:

$$\int_0^e \alpha^T K_p d\alpha \rightarrow \infty \quad \text{as } \|e\| \rightarrow \infty \quad (43)$$

Next, since $V(e, \dot{e})$ is positive definite and radially unbounded, then we can evaluate its time derivative along the trajectory of the resulting closed-loop dynamics as follows:

$$\dot{V}(e, \dot{e}) = \dot{e}^T \ddot{e} + e^T K_p \dot{e} \quad (44)$$

Substituting (39) into (44) yields:

$$\dot{V}(e, \dot{e}) = \dot{e}^T [M^*(\eta)^{-1} w_{ext}(t) - K_p e - K_d \dot{e}] + e^T K_p \dot{e} \quad (45)$$

which, we can rewritten as follows:

$$\dot{V}(e, \dot{e}) = -[\dot{e}^T K_d \dot{e} - \dot{e}^T M^*(\eta)^{-1} w_{ext}(t)] \quad (46)$$

From (46), and based on Assumption 1, K_d can be designed to compensate for the effect of $w_{ext}(t)$ as follows:

$$K_{id} > \frac{\|w_{ext}(t)\|}{\min_i |\lambda_i\{M^*(\eta)\}| \|\dot{e}\|}, \quad i = \overline{1, 6} \quad (47)$$

where $K_d = \text{diag}\{k_{1d}, k_{2d}, \dots, k_{6d}\}$.

Finally, from (46) we can deduce that $\dot{V}(e, \dot{e})$ is negative semidefinite if argument (47) is satisfied. This leads to the conclusion that the origin of the closed-loop dynamics is asymptotically stable based on LaSalle's invariance principle.

3.3 Control solution 3: Adaptive Model-based Tracking Control Scheme

Even though having complete or partial knowledge of the system dynamics improves the performance of the control scheme, the process of obtaining an accurate model which represents system remains a challenging task. Similarly, tracking control of a low-inertia underwater vehicle with a model-based controller may result in a high tracking error due to its challenging modelling process, in addition to the variations of the vehicle's parameters as well as the unpredictable nature of the underwater environments. Besides, the parametric variations, the high sensitivity of low-inertia underwater vehicles, the inherently coupled nonlinearities in their dynamics drastically affect the control schemes performances during marine missions. To deal with these issues, the designed controllers for such vehicles should dynamically adjust themselves to neutralise these effects in real-time. In the field of

control systems, any controller with auto-adjustment mechanism is referred to as an adaptive controller [2]. Hence, an adaptive control technique can be considered as a process of designing a control scheme with an auto-adjustment mechanism for a dynamical system under the influence of parametric uncertainties in high precision applications [40]. However, the adaptive control scheme design requires accurate knowledge of the system dynamics structure, which is used to characterise the uncertainty of the system as a set of unknown parametric terms; this may help to facilitate the controller design. The adaptive control scheme can be categorised as a direct adaptive control technique or an indirect adaptive control technique. The direct adaptive control technique deals with direct estimation of the control parameters which are used to modify the system's dynamics. However, the indirect adaptive control technique involves the estimation of the system's dynamics, which is used in the design of the controller. For the case of our underwater vehicle in this section, we focus on the implementation of an adaptive version of PD+ controller (APD+) for trajectory tracking. This controller is designed and implemented on the vehicle subsequently.

3.3.1 Background on the APD+ control scheme and its application on Leonard underwater vehicle

A PD control structure combined with desire compensation terms, obtained from a system dynamics as well as a predefined desired trajectory in tracking control, is known as a PD+ control scheme. Besides, its implementation simplicity in real-time applications, the compensation terms in the control law can be computed offline to reduce computational cost once the desired trajectory is defined [40]. Considering these advantages of the PD+ control scheme, we modify its structure by adding an adaptation to improve its robustness. The improved control scheme is implemented on the highly uncertain dynamical model with a nonlinear coupled behaviour of Leonard underwater vehicle. The design and implementation of this control law as well as its adaptation mechanism for Leonard underwater vehicle are given as follows:

$$\tau = J^T(\eta) \left[M^*(\eta)\ddot{\eta}_d + C^*(v, \eta)\dot{\eta}_d + D^*(v, \eta)\dot{\eta}_d - \left[\Phi_\theta \hat{\theta}^T + K_p e(t) + K_d \frac{de(t)}{dt} \right] \right] \quad (48)$$

$$\dot{\hat{\theta}} = \Gamma_\theta^{-1} \Phi_\theta \left[\alpha e(t) + \frac{de(t)}{dt} \right] \quad (49)$$

where $\tau = [\tau_x, \tau_y, \tau_z, \tau_\phi, \tau_\theta, \tau_\psi]^T$ is the vector of the six control inputs of the vehicle, $J(\eta)$ is a matrix which defines three dimensional spatial-transformation between the earth-fixed frame and vehicle's body-fixed frame, $M^*(\eta)$ defines the inertia matrix including the added mass effects, $C^*(v, \eta)$ represents the Coriolis and centripetal matrix, $D^*(v, \eta)$ is the hydrodynamic damping matrix including both linear and quadratic effects, $e(t)$ is the vector of the tracking errors, $K_p = \text{diag}\{k_{1p}, k_{2p}, \dots, k_{6p}\} > 0$ and $K_d = \text{diag}\{k_{1d}, k_{2d}, \dots, k_{6d}\} > 0$ are the feedback gains, $\alpha > 0$, $\Gamma_\theta^{-1} = \text{diag}\{\gamma_1, \gamma_2, \dots, \gamma_6\} > 0$ is the adaptation gain matrix, Φ_θ is the regressor matrix and θ is the vector of the unknown parameters to be estimated by the controller.

The dynamics of Leonard underwater vehicle is characterised by its linearity with respect

to the dynamic parameters. We exploit this property of the vehicle's dynamics and focus on designing Φ_θ and θ based on the terms (i.e. $w_{ext}(t)$ and $g^*(\eta)$) which significantly affect the steady-state of the vehicle as follows [35] [41]:

$$\Phi_\theta = \begin{bmatrix} \Phi_g & \Phi_{w_{ext}} \end{bmatrix} \quad \text{with} \quad \Phi_g = \begin{bmatrix} s\theta & & & & & \\ -c\theta s\phi & 0_{3 \times 1} & & & & \\ -c\theta c\phi & & & & & \\ & & & -c\theta s\psi & & \\ 0_{3 \times 1} & & & -s\theta & & \\ & & & & 0 & \end{bmatrix} \quad \text{and} \quad \Phi_{w_{ext}} = J(\eta) \quad (50)$$

and

$$\hat{\theta}^T = \begin{bmatrix} \hat{\theta}_g^T & \hat{\theta}_{w_{ext}}^T \end{bmatrix}^T \quad \text{with} \quad \hat{\theta}_g^T = [f_B \quad z_b B]^T \quad \text{and} \quad \hat{\theta}_{w_{ext}}^T = [w_x, w_y, w_z, 0, 0, 0]^T \quad (51)$$

where Φ_g and $\Phi_{w_{ext}}$ are the regressor matrices of $g^*(\eta)$ and $w_{ext}(t)$ respectively, while $\hat{\theta}_g^T$ and $\hat{\theta}_{w_{ext}}^T$ are the estimates of the unknown dynamic parameters of $g^*(\eta)$ and $w_{ext}(t)$ respectively. Further, $w_{ext}(t)$ is considered as a water current with irrotational components w_x , w_y and w_z in earth-fixed frame.

The structure of the proposed APD+ control scheme implemented on Leonard underwater vehicle is illustrated in Figure 5.

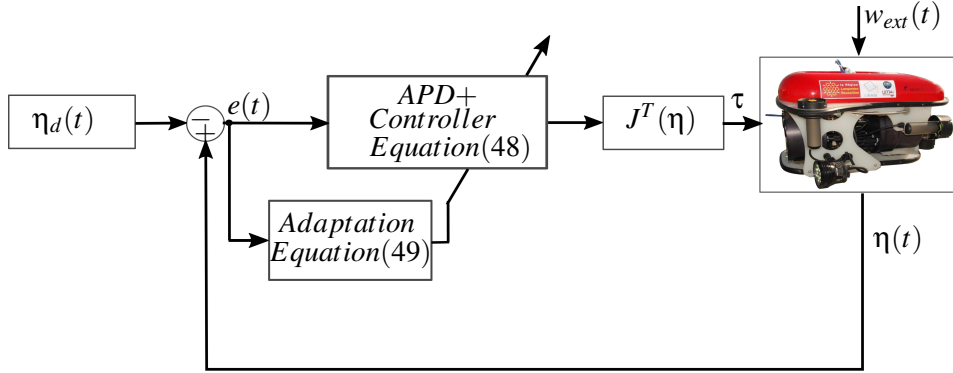


Figure 5: Block diagram of APD+ control scheme implemented on Leonard underwater vehicle.

3.3.2 Stability analysis

For the ease of the stability analysis, we substitute the controller (48) into the vehicle's dynamics (20) and write the resulting closed-loop dynamics in a state-space form as follows:

$$\frac{d}{dt} \begin{bmatrix} e \\ \dot{e} \\ \hat{\theta} \end{bmatrix} = \begin{bmatrix} \dot{e} \\ M^*(\eta)^{-1} \left[-C^*(v, \eta) \dot{e} - D^*(v, \eta) \dot{e} - g^*(\eta) + w_{ext}(t) - \Phi_\theta \hat{\theta}^T - K_p e - K_d \dot{e} \right] \\ \Gamma_\theta^{-1} \Phi_\theta [\alpha e + \dot{e}] \end{bmatrix} \quad (52)$$

Next, we consider the following Lyapunov candidate function:

$$V(e, \dot{e}, \tilde{\theta}) = \frac{1}{2} \dot{e}^T M^*(\eta) \dot{e} + \frac{1}{2} \tilde{\theta}^T \Gamma_{\theta} \tilde{\theta} + \int_0^e \alpha^T K_p d\alpha \quad (53)$$

The proposed Lyapunov candidate function in (53) is positive definite and radially unbounded since the first two terms are positive definite, and the integral term satisfies the following arguments:

$$\int_0^e \alpha^T K_p d\alpha = \int_0^{e_1} \alpha_1^T k_{1p} d\alpha_1 + \int_0^{e_2} \alpha_2^T k_{2p} d\alpha_2 + \dots + \int_0^{e_6} \alpha_6^T k_{6p} d\alpha_6 \quad (54)$$

$$\int_0^e \alpha^T K_p d\alpha > 0, \quad \forall e \neq 0 \in \mathbb{R}^n \quad (55)$$

where $K_p = \text{diag}\{k_{1p}, k_{2p}, \dots, k_{6p}\}$.

From arguments (54) and (55) above, we can conclude that:

$$\int_0^e \alpha^T K_p d\alpha \rightarrow \infty \quad \text{as } \|e\| \rightarrow \infty \quad (56)$$

Then, the time derivative of (53) can be written as follows:

$$\dot{V}(e, \dot{e}, \tilde{\theta}) = \dot{e}^T M^*(\eta) \ddot{e} + \frac{1}{2} \dot{e}^T \dot{M}^*(\eta) \dot{e} + \tilde{\theta}^T \Gamma_{\theta} \dot{\tilde{\theta}} + e^T K_p \dot{e} \quad (57)$$

By substituting the closed-loop dynamics (52) into the time derivative of the Lyapunov candidate function (57), we deduce:

$$\begin{aligned} \dot{V}(e, \dot{e}, \tilde{\theta}) = \dot{e}^T \left[-C^*(v, \eta) \dot{e} - D^*(v, \eta) \dot{e} - g^*(\eta) + w_{ext}(t) - \Phi_{\theta} \hat{\theta}^T - K_p e - K_d \dot{e} \right] \\ + \frac{1}{2} \dot{e}^T \dot{M}^*(\eta) \dot{e} + \tilde{\theta}^T \Gamma_{\theta} \dot{\tilde{\theta}} + e^T K_p \dot{e} \end{aligned} \quad (58)$$

Since we design the adaptation law of the controller based on the terms which affect the steady-state of the vehicle, that is, $w_{ext}(t)$ and $g^*(\eta)$, then these terms can be rewritten in a regressor form as follows:

$$w_{ext}(t) - g^*(\eta) = \Phi_{\theta} \theta^T \quad (59)$$

Then, substituting (59) into (58) leads to:

$$\begin{aligned} \dot{V}(e, \dot{e}, \tilde{\theta}) = -\dot{e}^T [D^*(v, \eta) \dot{e} + K_d] \dot{e} + \frac{1}{2} \dot{e}^T [\dot{M}^*(\eta) - 2C^*(v, \eta)] \dot{e} + \dot{e} \Phi_{\theta} [\theta^T - \hat{\theta}^T] \\ - \tilde{\theta}^T \Gamma_{\theta} \dot{\tilde{\theta}} \end{aligned} \quad (60)$$

Injecting the adaptation law (49) into (60) above, leads to:

$$\begin{aligned} \dot{V}(e, \dot{e}, \tilde{\theta}) = -\dot{e}^T [D^*(v, \eta) \dot{e} + K_d] \dot{e} + \frac{1}{2} \dot{e}^T [\dot{M}^*(\eta) - 2C^*(v, \eta)] \dot{e} + \dot{e} \Phi_{\theta} [\theta^T - \hat{\theta}^T] \\ - \tilde{\theta}^T \Gamma_{\theta} \left[\Gamma_{\theta}^{-1} \Phi_{\theta} [\alpha e + \dot{e}] \right] \end{aligned} \quad (61)$$

Then, (61) can be rewritten as follows:

$$\begin{aligned} \dot{V}(e, \dot{e}, \tilde{\theta}) = & -\dot{e}^T [D^*(v, \eta)\dot{e} + K_d]\dot{e} + \frac{1}{2}\dot{e}^T [M^*(\eta) - 2C^*(v, \eta)]\dot{e} + \dot{e}\Phi_\theta\tilde{\theta}^T \\ & -\tilde{\theta}^T\Phi_\theta\alpha e - \tilde{\theta}^T\Phi_\theta\dot{e} \end{aligned} \quad (62)$$

Based on Assumption 2 and the fact that $C^*(v, \eta)$ is skew symmetric, then we can rewrite (62) as follows:

$$\dot{V}(e, \dot{e}, \tilde{\theta}) = -\dot{e}^T [D^*(v, \eta)\dot{e} + K_d]\dot{e} - \tilde{\theta}^T\Phi_\theta\alpha e \quad (63)$$

From (63) above, it is possible to conclude that $\dot{V}(e, \dot{e}, \tilde{\theta})$ is negative definite; additionally, $D^*(v, \eta) > 0$ and $K_d > 0$, and the second term on the right-hand side of $\dot{V}(e, \dot{e}, \tilde{\theta})$, is negative. Even if, the second term on the right-hand side of $\dot{V}(e, \dot{e}, \tilde{\theta})$ changes the sign due to the possible high degree of uncertainty on the external disturbance, then α can be designed so that the effect of this second term becomes negligible, while the first term dominates the right-hand side of $\dot{V}(e, \dot{e}, \tilde{\theta})$. Consequently, $\dot{V}(e, \dot{e}, \tilde{\theta})$ will remain negative definite despite the influence of these effects. Therefore, we can conclude that the origin of the resulting closed-loop dynamics is asymptotically stable.

4 Simulation Results: A Comparative Study

To compare the effectiveness and robustness of the proposed three controllers designed in the previous section, we implemented them on Leonard underwater vehicle described in section 2. During the implementation process of the control schemes, various scenarios-based numerical simulations have been conducted and the obtained results are discussed in the sequel. Before discussing the obtained results, the proposed simulation scenarios are introduced.

4.1 Proposed Numerical Simulations Scenarios

The following scenarios are tested to evaluate the effectiveness and robustness of all the proposed three control schemes on Leonard low-inertia underwater vehicle:

Scenario 1 (nominal case): The main objective of this scenario is to obtain the best control feedback gains, which will result in the best vehicle's desired trajectory tracking. The obtained gains are used in the remaining scenarios without any modification.

Scenario 2 (external disturbance rejection): In this scenario, we consider the presence of water current and the task of transporting an object by the vehicle from a first point and dropping it at another point as an external disturbance. The ability of each controller to reject this disturbance and keep the vehicle on the desired trajectory is evaluated. Indeed, the task of transporting the object and dropping it at a specific desired depth is illustrated in Figure 6.

Scenario 3 (robustness toward vehicle's damping and buoyancy changes): The main objective of this scenario is to evaluate the robustness of each controller toward parametric variations such as the modifications of the vehicle's buoyancy and damping.

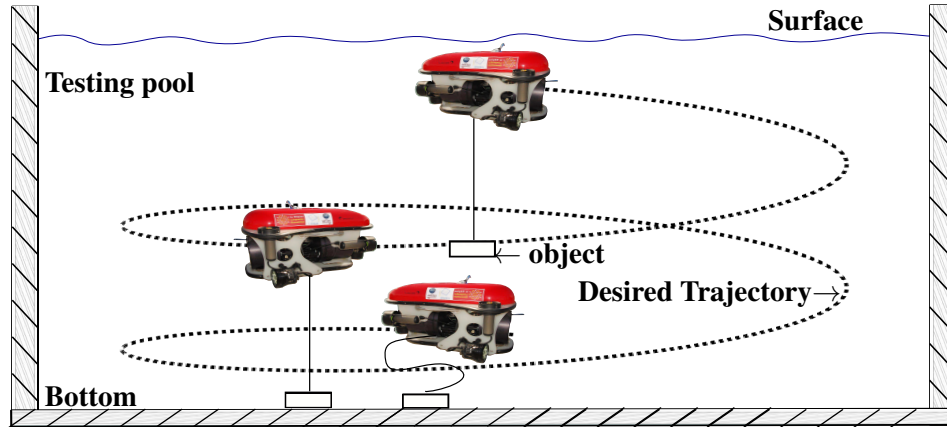


Figure 6: Illustration of Leonard underwater vehicle following a predefined desired helical trajectory while carrying an object from the surface and dropping it at the bottom of the testing pool.

4.2 Nominal scenario (Results and discussion)

In this simulation test, defined previously as Scenario 1, the vehicle is intended to follow a predefined 3D helical desired trajectory under the influence of internal disturbances such as sensor noise; external disturbances and parametric uncertainties are not considered in order to obtain the best feedback gains to be used in forthcoming scenarios. The obtained results are depicted in Figures 7- 11. The three controllers are able to guide the vehicle to follow the desired 3D helical trajectory from the initial position ($\approx 0m$) to a depth of approximately $13m$, which is near to the bottom of the testing pool. The vehicle completes this mission in $720s$ and remains stable near to the bottom of the testing pool.

Besides the complex nature of the chosen trajectory, it has a medium radius ($\approx 4m$), which helps us to evaluate the robustness and effectiveness of the proposed controllers to manoeuvre the vehicle in tracking the desired helical trajectory. The six degrees of freedom, namely, surge and roll, sway and pitch as well as heave and yaw evolution versus time are shown in Figure 7 (top plots), Figure 8 (top plots) and Figure 9 (top plots), respectively. Figure 10 shows the tracking results in 3D, which can help to visualise the motion of the vehicle in 3D easily during this test. Moreover, one can observe from Figure 7 (top left plot), Figure 8 (top left plot) and Figure 9 (top left plot) under this scenario, that all the three controllers effectively guide the vehicle to track the desired trajectory in the surge, sway and heave, respectively.

Similarly, regarding the vehicle's attitude tracking, the proposed controllers guide the vehicle to track the desired roll and pitch with slight tracking errors as shown in Figure 7 (top right plot) and Figure 8 (top right plot). However, the roll and pitch tracking errors for the PID are slightly bigger as shown in Figure 7 (top right plot) and Figure 8 (top right plot), respectively. These slightly bigger tracking errors of the proposed PID controller can also be noticed in Figures 7- 8 (middle right plot). Concerning the yaw tracking all the proposed three controllers are able to track the desired yaw as shown in Figure 9 (top right plot). Also, the tracking errors of the proposed controllers in all the six degrees of

Table 2: Summary of the controllers performance indices

		PID	CT	APD+
RMSE 3D-position [m]	Nominal Scenario	0.1133	0.0944	0.0618
	Combine Scenarios	0.5421	0.1382	0.1462
RMSE 3D-orientation [deg]	Nominal Scenario	2.4026	0.9038	0.4618
	Combine Scenarios	2.4108	0.9176	0.4629

freedom of the vehicle are shown in Figures 7- 9 (middle plots). To numerically evaluate the tracking performances of the proposed controllers for position and orientation tracking of the vehicle, we use a performance index in 3D known as root mean square error (RMSE) expressed as follows:

$$RMSE(3D \text{ position/orientation}) = \left[\frac{1}{N} \sum_{i=1}^N \left[e_{x/\phi}^2(i) + e_{y/\theta}^2(i) + e_{z/\psi}^2(i) \right] \right]^{\frac{1}{2}} \quad (64)$$

where N denotes the number of time-samples, while $e_{x/\phi}$, $e_{y/\theta}$ and $e_{z/\psi}$ are the tracking errors in position and orientation on x, y and z axes, respectively.

Using (64) above, we compute the RMSE for both 3D position and orientation of the controllers; the results of the computations are summarised in Table 2. Next, the control inputs evolution of all the six degrees of freedom of the vehicle for all the controllers are depicted in Figures 7- 9 (bottom plots). Then, from the control signals evolution versus time obtained results, we numerically estimate the energy consumption of each controller using the following index:

$$INT = \int_{t_1}^{t_2} \|\tau(t)\| dt \quad (65)$$

where INT defines the integral of control signals, $t_1 = 1s$ and $t_2 = 720s$

Since CT and APD+ controllers show superior tracking performances, confirmed by Table 2, we investigate their energy consumption using (65) as follows:

$$\frac{INT_{3D \text{ position APD+}}}{INT_{3D \text{ position CT}}} = \frac{7130}{7005} = 1.02. \quad \frac{INT_{3D \text{ orientation APD+}}}{INT_{3D \text{ orientation CT}}} = \frac{209}{214} = 0.98. \quad (66)$$

From (66) it is worth to note, that besides the superior tracking performance of the APD+ controller, its energy consumption is approximately the same as the CT controller in both desired position and orientation trackings. Hence, we can conclude that the APD+ controller demonstrates superior tracking performance than both the CT and PID controllers in this scenario. The uncertain parametric estimations made by the APD+ controller are shown in Figure 11.

4.3 Combined Scenarios (Results and discussion)

To investigate the robustness of each controller in this test, we propose to combine all the scenarios defined previously in one test, and the vehicle follows the same desired trajectory

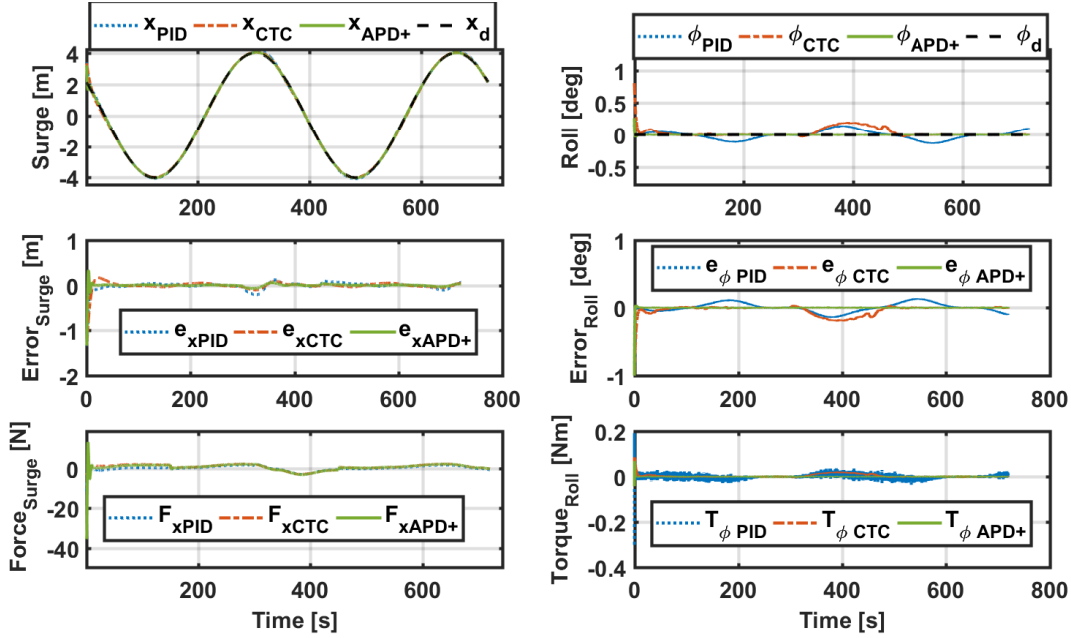


Figure 7: Trackings performances comparison of the APD+, CT and PID controllers implemented on Leonard underwater vehicle in the nominal scenario: (upper plots) surge and roll trackings, (middle plots) surge and roll corresponding tracking errors and (bottom plots) are the evolution of the vehicle's control inputs.

as in the nominal case. The effect of sensor measurement noise can be noticed in Figures 12-14 (bottom plots), but more amplified on the roll and pitch control signals of the proposed APD+ controller. When the vehicle reaches a depth of 2.5m, the influence of a 3-kg object tied at the bottom of the vehicle becomes active as illustrated in Figure 6. We can notice the effect of this added mass as a sudden change in the overall mass of the vehicle at 150s along the heave axis as shown in Figure 14 (heave plots), which can also be visualised in 3D as shown in Figure 15; however, the vehicle yaw tracking is less affected as illustrated in Figure 14 (yaw plots).

In the case of CT controller, the vehicle deviates slightly from the desired trajectory, while the APD+ controller compensates for the effect within a short time (about 4s) and keeps the vehicle around the desired trajectory; on the other hand, it takes the PID controller about 40s to compensate for the same effect. Also, the vehicle tracking is less affected on the surge, roll and sway in the case of the proposed APD+ controller as compared to the remaining controllers, as shown in Figure 12 and Figure 13 (sway plots). However, the pitch tracking of the proposed APD+ controller is slightly affected as shown in Figure 12 (pitch plots).

When the vehicle reaches 5m of depth, its damping and floatability are modified by +90% and +200%, respectively, to evaluate the robustness of the three controllers toward parametric variations of the vehicle, which is clearly seen in Figure 12 (roll plots), Figure 13 (pitch plots) and Fig 14 (heave plots) at about 300s. Concerning the roll and pitch tracking APD+ controller compensates for this effect and keeps the vehicle very close to

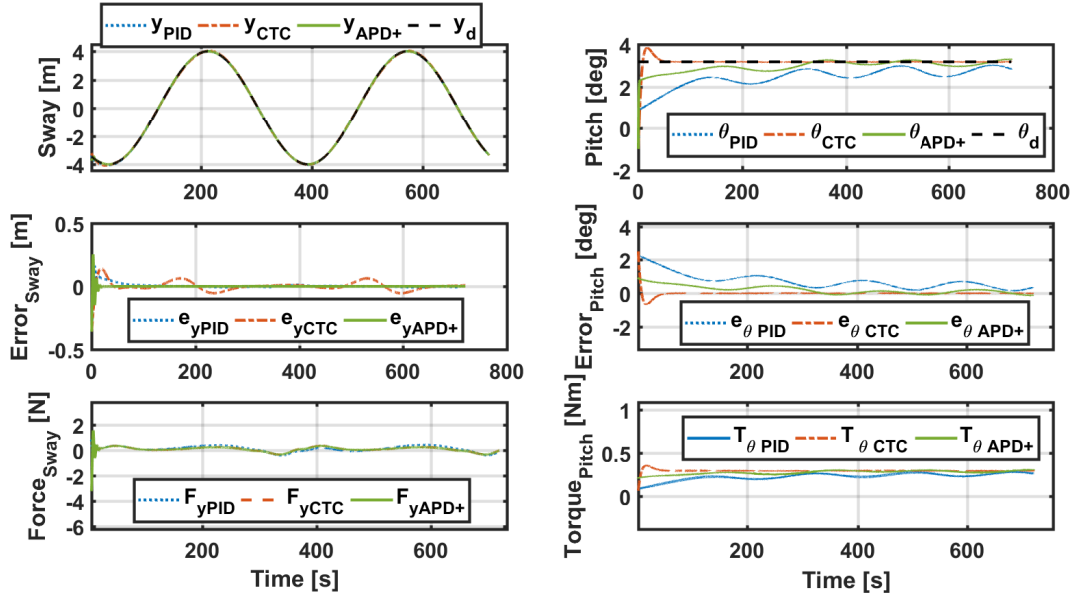


Figure 8: Trackings performances comparison of the APD+, CT and PID controllers implemented on Leonard underwater vehicle in the nominal scenario: (upper plots) sway and pitch trackings, (middle plots) sway and pitch corresponding tracking errors and (bottom plots) are the evolution of the vehicle's sway and pitch control inputs.

the desired trajectory. At the same time, it takes the CT controller about 20s and 15s to compensate for the same effect on roll and pitch, respectively. However, the PID controller oscillates slightly around the desired roll, while tracking the desired pitch with a slightly bigger tracking error.

As the vehicle reaches the depth of about 7.5m in 450, the 3-kg object tied to the vehicle touches the floor of the testing pool at the same time the vehicle's damping and floatability are recharged to their nominal values. These effects are clearly observed in Figure 12 (roll plots), Figure 13 (pitch plots) and Figure 14 (heave plots), as well as in Figure 15 (3D plot), while all the three controllers maintain approximately their superior performances in the surge, sway and yaw trackings as shown in Figure 12 (surge plots), Figure 13 (sway plots) and Figure 14 (yaw plots), respectively.

To further evaluate the ability of the controllers to reject external disturbances, when the vehicle goes to 10m depth, we apply a water current moving at a speed of 0.35m/s to disturb the vehicle. Even though, the controllers reject the applied external disturbance, but as a consequence the controllers consume a slightly higher amount of energy especially the CT controller as shown in Figure 12 ($Force_{surge}$ plot), Figure 13 ($Force_{sway}$ plot) and Figure 14 ($Force_{heave}$ plot).

Finally, it is possible to conclude that the APD+ controller demonstrates superior performance as compared to the CT and PID controllers. Even though the CT controller shows similar performance to APD+ controller in terms of 3D position tracking confirmed by numerical computation of RMSE given in Table 2, the RMSE of APD+ controller for 3D orientation tracking from Table 2 is 50% less than the RMSE of CT controller. Moreover,

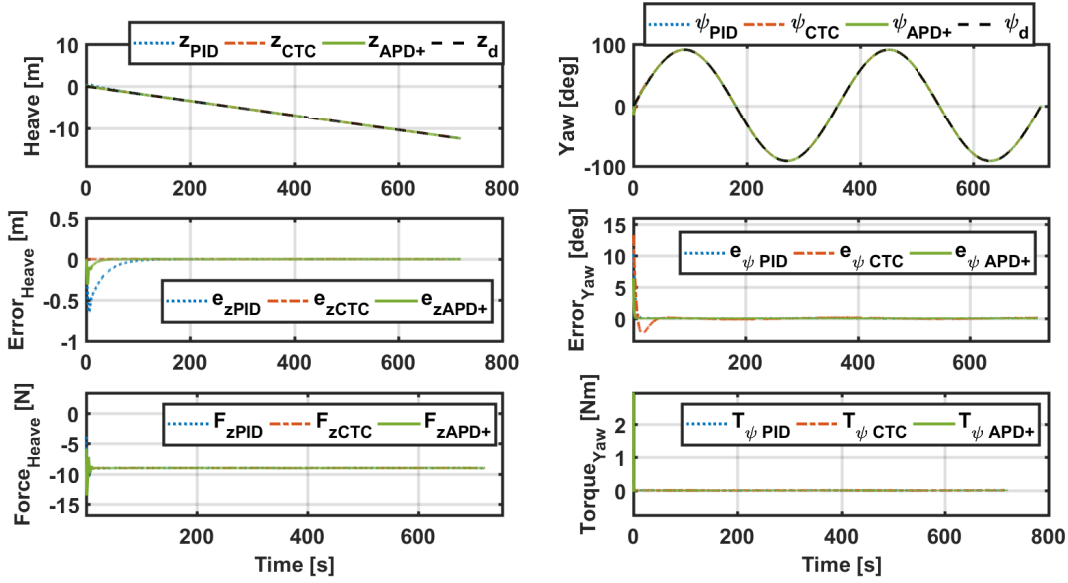


Figure 9: Trackings performances comparison of the APD+, CT and PID controllers implemented on Leonard underwater vehicle in the nominal scenario: (upper plots) heave and yaw trackings, (middle plots) heave and yaw corresponding tracking errors and (bottom plots) are the evolution of the vehicle's heave and yaw control inputs.

the energy consumption estimation using (65) shows that approximately the same energy is consumed by both APD+ and CT controllers during 3D position trackings. However, concerning 3D orientation tracking, the APD+ controller consumes 3.5% less energy than the CT controller. The uncertain parametric and external disturbance estimations by the APD+ controller are depicted in Figures 16 and 17, respectively. From these figures representing uncertain parametric and external disturbance estimations by the APD+ controller, one can observe the influence of all the effects introduced during this simulation scenario.

5 Conclusion and Future Work

In this chapter, the performances of the non-model-based (PID), the model-based (CT) as well as the adaptive model-based (APD+) controllers have been investigated for three-dimensional (3D) helical trajectory tracking of a low-inertia underwater vehicle. The resulting closed-loop dynamics stability analysis of all the three proposed controllers have been conducted based on Lyapunov direct method. The controllers have then been implemented on Leonard underwater vehicle for 3D helical trajectory tracking. Scenarios-based simulation results demonstrate the superior performance of APD+ controller, compared to the two other controllers, for marine applications under the influences of parametric variations, internal vehicle's perturbations and external disturbances. In the near future, we will focus on implementing these control schemes in real-time on low-inertia underwater vehicles. Also, we may integrate observers in real-time to all the controllers for velocity estimation, since the majority of the low-inertia and

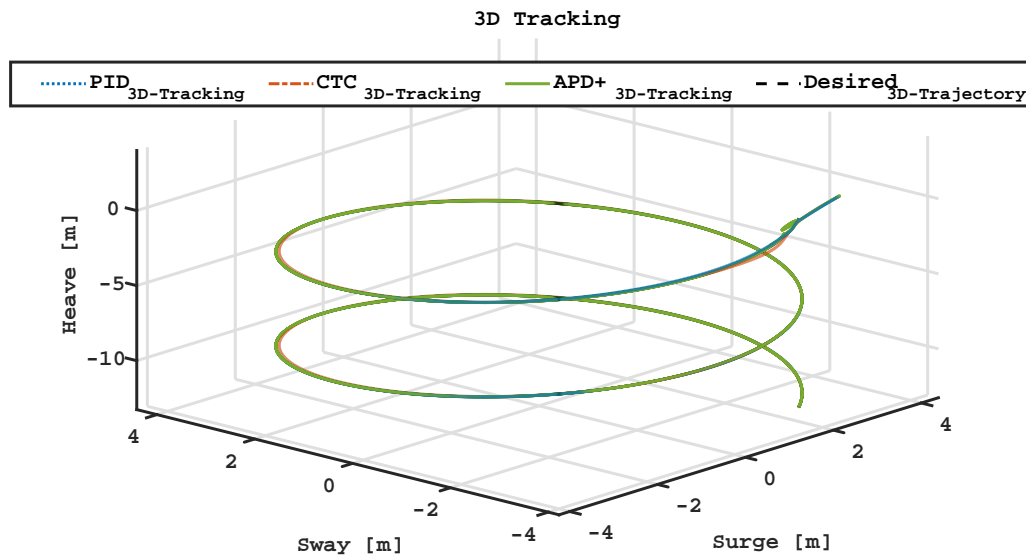


Figure 10: Three-dimensional (3D) helical trajectory trackings performances comparison of the APD+, CT and PID controllers implemented on Leonard underwater vehicle in the nominal scenario.

low-cost underwater vehicles are not equipped with DVL (Doppler velocity logger) sensors.

Acknowledgments

The authors thanks the Petroleum Technology Development Fund (PTDF), Nigeria, for supporting the first author financially through PhD scholarship.

References

- [1] J. Bao, D. Li, X. Qiao, and T. Rauschenbach, "Integrated navigation for autonomous underwater vehicles in aquaculture: A review," *Information Processing in Agriculture*, 2019.
- [2] D. Maalouf, A. Chemori, and V. Creuze, "L1 adaptive depth and pitch control of an underwater vehicle with real-time experiments," *Ocean Engineering*, vol. 98, pp. 66–77, 2015.
- [3] A. Sahoo, S. K. Dwivedy, and P. Robi, "Advancements in the field of autonomous underwater vehicle," *Ocean Engineering*, vol. 181, pp. 145–160, 2019.
- [4] S. K. Chaturvedi, S. Basu, and S. Banerjee, "Gimbal orientation study and assessment for the autonomous underwater vehicles," *Journal of Ocean Engineering and Science*, 2019.
- [5] G. Antonelli, *Underwater robots*, vol. 123. Springer, 2018.

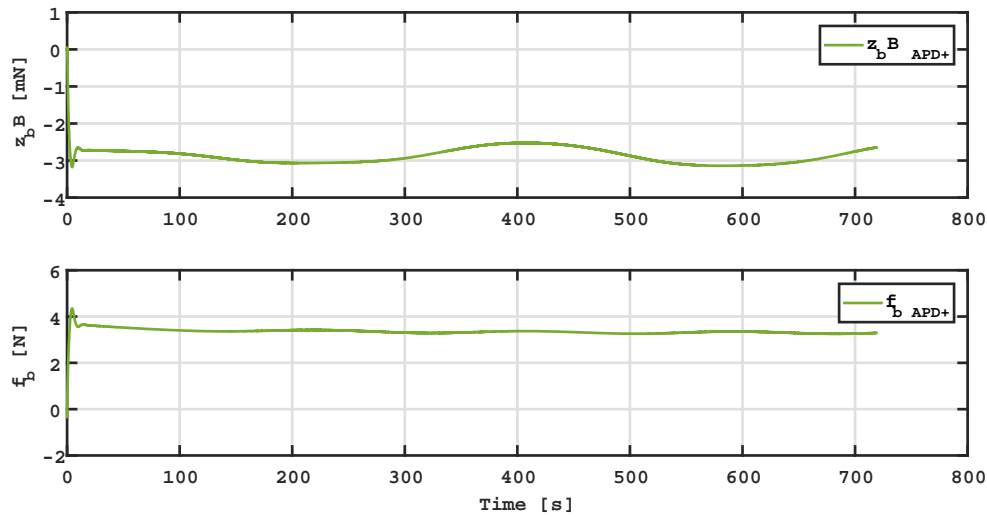


Figure 11: Parametric estimations of the APD+ controller implemented on Leonard underwater vehicle for three-dimensional (3D) helical trajectory tracking in the nominal scenario.

- [6] F. Kong, Y. Guo, and W. Lyu, “Dynamics modeling and motion control of a new unmanned underwater vehicle,” *IEEE Access*, vol. 8, pp. 30119–30126, 2020.
- [7] S. T. Havenström, A. Rasheed, and O. San, “Deep reinforcement learning controller for 3d path-following and collision avoidance by autonomous underwater vehicles,” 2020.
- [8] J. Guerrero, J. Torres, V. Creuze, and A. Chemori, “Adaptive disturbance observer for trajectory tracking control of underwater vehicles,” *Ocean Engineering*, vol. 200, p. 107080, 2020.
- [9] M. M. Hammad, A. K. Elshenawy, and M. El Singaby, “Position control and stabilization of fully actuated auv using pid controller,” in *Proceedings of SAI Intelligent Systems Conference*, pp. 517–536, Springer, 2016.
- [10] S. A. Watson and P. N. Green, “Depth control for micro-autonomous underwater vehicles (μ auvs): Simulation and experimentation,” *International Journal of Advanced Robotic Systems*, vol. 11, no. 3, p. 31, 2014.
- [11] C.-L. Kuo, C.-K. Tsui, N.-S. Pai, C.-H. Lin, S.-C. Chen, and P.-W. Li, “A pid controller for the underwater robot station-keeping,” in *2016 IEEE 14th International Conference on Industrial Informatics (INDIN)*, pp. 1242–1246, IEEE, 2016.
- [12] V. Upadhyay, S. Gupta, A. Dubey, M. Rao, P. Siddhartha, V. Gupta, S. George, R. Bobba, R. Sirikonda, A. Maloo, *et al.*, “Design and motion control of autonomous underwater vehicle, amogh,” in *2015 IEEE Underwater Technology (UT)*, pp. 1–9, IEEE, 2015.

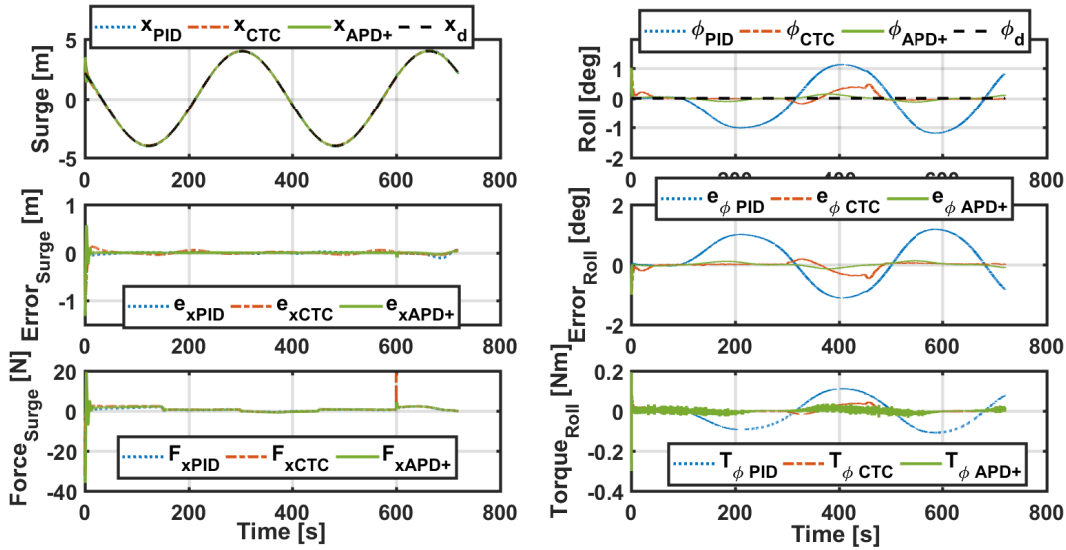


Figure 12: Trackings performances comparison of the APD+, CT and PID controllers implemented on Leonard underwater vehicle in the combined scenario: (upper plots) surge and roll trackings, (middle plots) surge and roll corresponding tracking errors and (bottom plots) the evolution of the vehicle's control inputs.

- [13] J. D. Geder, J. Palmisano, R. Ramamurti, W. C. Sandberg, and B. Ratna, "Fuzzy logic pid based control design and performance for a pectoral fin propelled unmanned underwater vehicle," in *2008 International Conference on Control, Automation and Systems*, pp. 40–46, IEEE, 2008.
- [14] B. Hu, H. Tian, J. Qian, G. Xie, L. Mo, and S. Zhang, "A fuzzy-pid method to improve the depth control of auv," in *2013 IEEE International Conference on Mechatronics and Automation*, pp. 1528–1533, IEEE, 2013.
- [15] Q. Chen, T. Chen, and Y. Zhang, "Research of ga-based pid for auv motion control," in *2009 International Conference on Mechatronics and Automation*, pp. 4446–4451, IEEE, 2009.
- [16] J. Guerrero, J. Torres, V. Creuze, A. Chemori, and E. Campos, "Saturation based non-linear pid control for underwater vehicles: Design, stability analysis and experiments," *Mechatronics*, vol. 61, pp. 96–105, 2019.
- [17] R. Hernández-Alvarado, L. G. García-Valdovinos, T. Salgado-Jiménez, A. Gómez-Espinosa, and F. Fonseca-Navarro, "Neural network-based self-tuning pid control for underwater vehicles," *Sensors*, vol. 16, no. 9, p. 1429, 2016.
- [18] C. Makavita, H. Nguyen, and D. Ranmuthugala, "Fuzzy gain scheduling based optimally tuned pid controllers for an unmanned underwater vehicle," *International journal of conceptions on electronics and communication engineering*, vol. 2, no. 1, pp. 7–13, 2014.

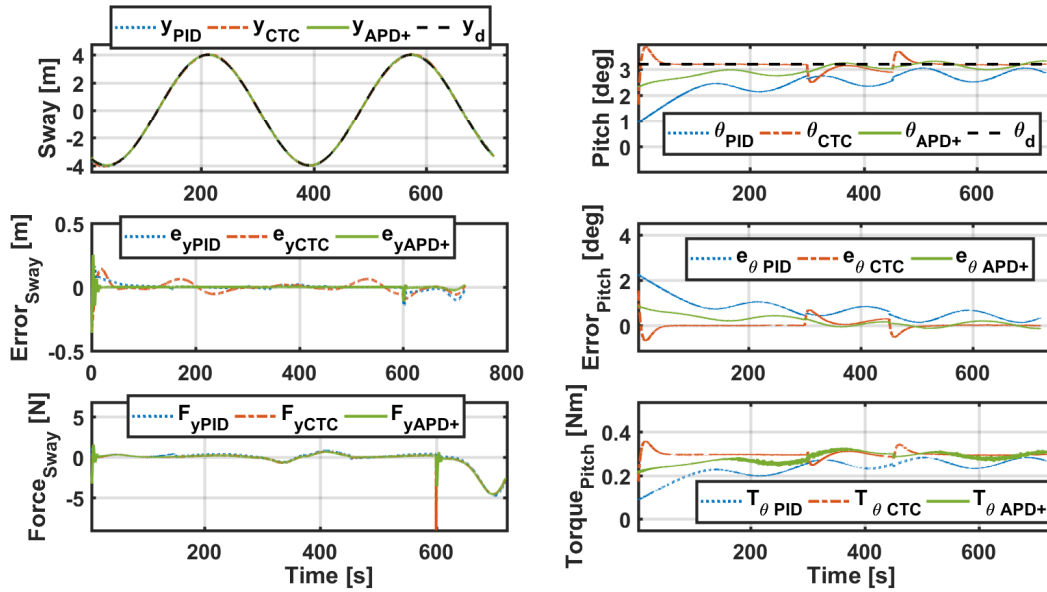


Figure 13: Trackings performances comparison of the APD+, CT and PID controllers implemented on Leonard underwater vehicle in the combined scenario: (upper plots) sway and pitch trackings, (middle plots) sway and pitch corresponding tracking errors and (bottom plots) are the evolution of the vehicle's sway and pitch control inputs.

- [19] L. Zhang, L. Liu, S. Zhang, and S. Cao, "Saturation based nonlinear fopd motion control algorithm design for autonomous underwater vehicle," *Applied Sciences*, vol. 9, no. 22, p. 4958, 2019.
- [20] E. Campos, J. Monroy, H. Abundis, A. Chemori, V. Creuze, and J. Torres, "A nonlinear controller based on saturation functions with variable parameters to stabilize an auv," *International Journal of Naval Architecture and Ocean Engineering*, vol. 11, no. 1, pp. 211–224, 2019.
- [21] N. Fischer, S. Bhasin, and W. Dixon, "Nonlinear control of an autonomous underwater vehicle: A rise-based approach," in *Proceedings of the 2011 American Control Conference*, pp. 3972–3977, IEEE, 2011.
- [22] J. Xu, M. Wang, and L. Qiao, "Dynamical sliding mode control for the trajectory tracking of underactuated unmanned underwater vehicles," *Ocean engineering*, vol. 105, pp. 54–63, 2015.
- [23] S. C. Martin and L. L. Whitcomb, "Nonlinear model-based tracking control of underwater vehicles with three degree-of-freedom fully coupled dynamical plant models: Theory and experimental evaluation," *IEEE Transactions on Control Systems Technology*, vol. 26, no. 2, pp. 404–414, 2017.
- [24] S. C. Martin and L. L. Whitcomb, "Fully actuated model-based control with six-degree-of-freedom coupled dynamical plant models for underwater vehicles: Theory

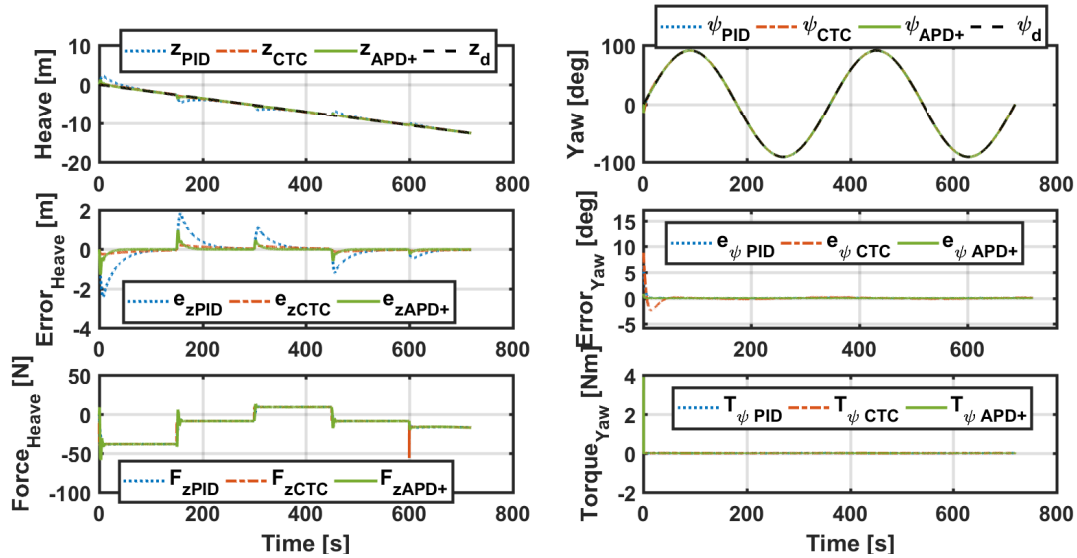


Figure 14: Trackings performances comparison of the APD+, CT and PID controllers implemented on Leonard underwater vehicle in the combined scenario: (upper plots) heave and yaw trackings, (middle plots) heave and yaw corresponding tracking errors and (bottom plots) are the evolution of the vehicle's heave and yaw control inputs.

and experimental evaluation,” *The International Journal of Robotics Research*, vol. 35, no. 10, pp. 1164–1184, 2016.

- [25] J. Xu and N. Wang, “Optimization of roV control based on genetic algorithm,” in *2018 OCEANS-MTS/IEEE Kobe Techno-Oceans (OTO)*, pp. 1–4, IEEE, 2018.
- [26] J. Chen, H. Zhu, L. Zhang, and Y. Sun, “Research on fuzzy control of path tracking for underwater vehicle based on genetic algorithm optimization,” *Ocean Engineering*, vol. 156, pp. 217–223, 2018.
- [27] A. A. R. Al Makdah, N. Daher, D. Asmar, and E. Shamma, “Three-dimensional trajectory tracking of a hybrid autonomous underwater vehicle in the presence of underwater current,” *Ocean Engineering*, vol. 185, pp. 115–132, 2019.
- [28] X. Liu, M. Zhang, and S. Wang, “Adaptive region tracking control with prescribed transient performance for autonomous underwater vehicle with thruster fault,” *Ocean Engineering*, vol. 196, p. 106804, 2020.
- [29] J. Guerrero, J. Torres, V. Creuze, and A. Chemori, “Trajectory tracking for autonomous underwater vehicle: An adaptive approach,” *Ocean Engineering*, vol. 172, pp. 511–522, 2019.
- [30] Y. Liao, T. Du, and Q. Jiang, “Model-free adaptive control method with variable forgetting factor for unmanned surface vehicle control,” *Applied Ocean Research*, vol. 93, p. 101945, 2019.

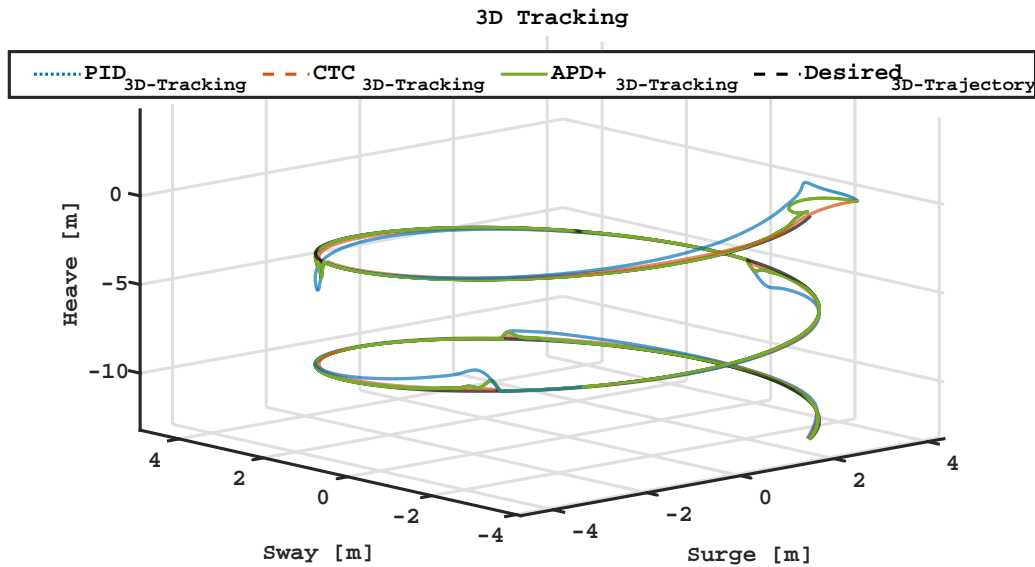


Figure 15: Three-dimensional (3D) helical trajectory trackings performances comparison of the APD+, CT and PID controllers implemented on Leonard underwater vehicle in the combined scenario.

- [31] Z. Zhang and Y. Wu, "Adaptive fuzzy tracking control of autonomous underwater vehicles with output constraints," *IEEE Transactions on Fuzzy Systems*, 2020.
- [32] Y. Lu, G. Zhang, L. Qiao, and W. Zhang, "Adaptive output-feedback formation control for underactuated surface vessels," *International Journal of Control*, vol. 93, no. 3, pp. 400–409, 2020.
- [33] S. Mohan and J. Kim, "Indirect adaptive control of an autonomous underwater vehicle-manipulator system for underwater manipulation tasks," *Ocean Engineering*, vol. 54, pp. 233–243, 2012.
- [34] E. Campos, A. Chemori, V. Creuze, J. Torres, and R. Lozano, "Saturation based non-linear depth and yaw control of underwater vehicles with stability analysis and real-time experiments," *Mechatronics*, vol. 45, pp. 49–59, 2017.
- [35] T. I. Fossen, "Guidance, navigation, and control of ships, rigs and underwater vehicles," *Trondheim, Norway: Marine Cybernetics*, 2002.
- [36] H. Saied, A. Chemori, M. El Rafei, C. Francis, and F. Pierrot, "From non-model-based to model-based control of pkms: a comparative study," in *Mechanism, Machine, Robotics and Mechatronics Sciences*, pp. 153–169, Springer, 2019.
- [37] P. Londhe, S. Mohan, B. Patre, and L. Waghmare, "Robust task-space control of an autonomous underwater vehicle-manipulator system by pid-like fuzzy control scheme with disturbance estimator," *Ocean Engineering*, vol. 139, pp. 1–13, 2017.

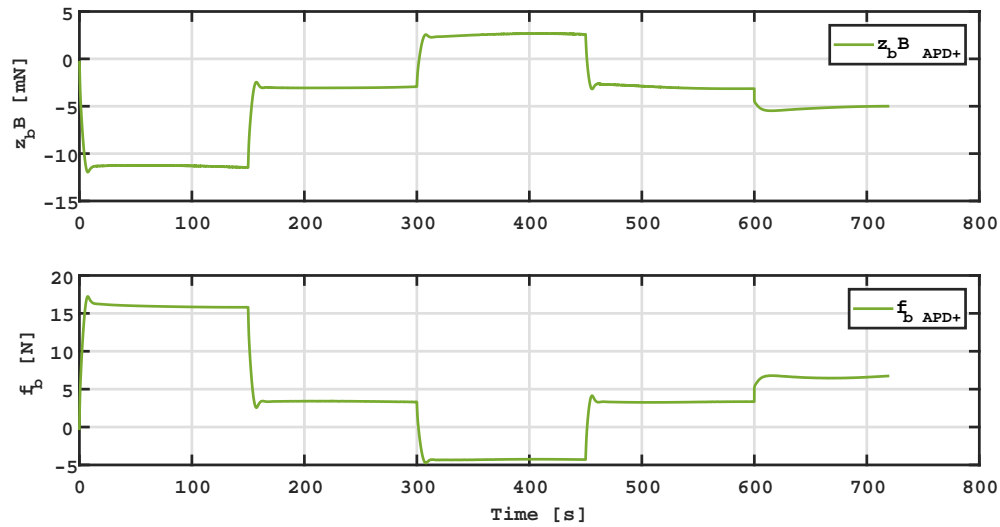


Figure 16: Parametric estimations of the APD+ controller implemented on Leonard underwater vehicle for three-dimensional (3D) helical trajectory tracking in the combined scenario.

- [38] M. Kim, H. Joe, J. Pyo, J. Kim, H. Kim, and S.-c. Yu, "Variable-structure pid controller with anti-windup for autonomous underwater vehicle," in *2013 OCEANS-San Diego*, pp. 1–5, IEEE, 2013.
- [39] H. Wu, W. Su, and Z. Liu, "Pid controllers: Design and tuning methods," in *2014 9th IEEE Conference on Industrial Electronics and Applications*, pp. 808–813, IEEE, 2014.
- [40] R. Kelly, V. S. Davila, and J. A. L. Perez, *Control of robot manipulators in joint space*. Springer Science & Business Media, 2006.
- [41] G. Antonelli, S. Chiaverini, N. Sarkar, and M. West, "Adaptive control of an autonomous underwater vehicle: experimental results on odin," *IEEE Transactions on Control Systems Technology*, vol. 9, no. 5, pp. 756–765, 2001.

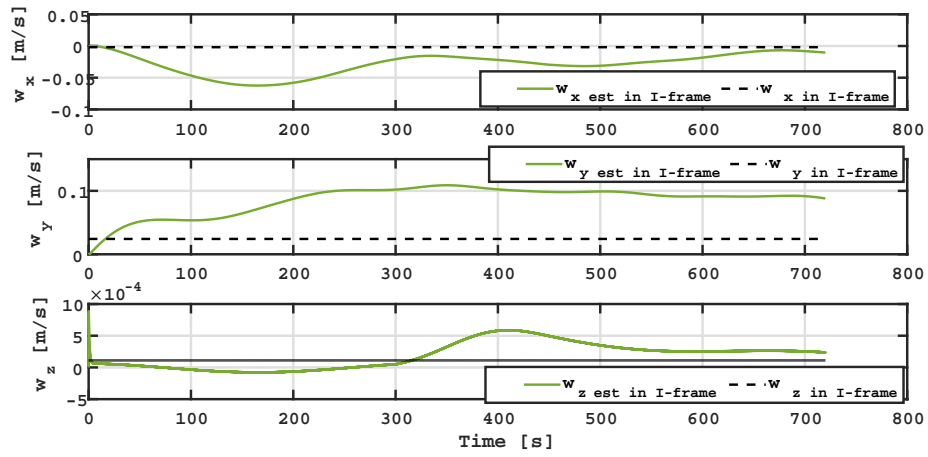


Figure 17: External disturbance estimation of the APD+ controller implemented on Leonard underwater vehicle for three-dimensional (3D) helical trajectory tracking in the combined scenario.